








# An Untargeted Survey of the Rotational Properties of Main-belt Asteroids using the Transiting Exoplanet Survey Satellite (TESS)

Andrew McNeill<sup>1,2</sup> , Michael Gowanlock<sup>2,3</sup> , Michael Mommert<sup>4,5</sup> , David E. Trilling<sup>2,3,5</sup> , Joe Llama<sup>5</sup> , and Nicholas Paddock<sup>1</sup>

<sup>1</sup> Department of Physics, Lehigh University, 16 Memorial Drive East, Bethlehem, PA 18015, USA; [andrew.mcneill@nau.edu](mailto:andrew.mcneill@nau.edu)

<sup>2</sup> Department of Astronomy and Planetary Science, Northern Arizona University, Flagstaff, AZ 86011, USA

<sup>3</sup> School of Informatics, Computing, and Cyber Systems, Northern Arizona University, Flagstaff, AZ 86011, USA

<sup>4</sup> University of St. Gallen, School of Computer Science, Rosenbergstrasse 30, 9000 St. Gallen, Switzerland

<sup>5</sup> Lowell Observatory, 1400 West Mars Hill Road, Flagstaff, AZ, 86001, USA

Received 2023 January 24; revised 2023 July 26; accepted 2023 July 28; published 2023 September 8

## Abstract

We present photometric data for minor planets observed by the Transiting Exoplanet Survey Satellite during its Cycle 1 operations. In total, we extracted usable detections for 37,965 objects. We present an examination of the reliability of the rotation period and light-curve amplitudes derived from each object based upon the number of detections and the normalized Lomb–Scargle power of our period fitting and compare and contrast our results with previous similar works. We show that for objects with 200 or more photometric detections and a derived normalized, generalized Lomb–Scargle power greater than 0.2, we have an 85% confidence in that period; this encompasses 3492 rotation periods we consider to be highly reliable. We independently examine a series of periods first reported by Pál et al.; periods derived in both works found to have similar results should be considered reliable. Additionally, we demonstrate the need to properly account for the true proportion of slow rotators ( $P > 100$  hr) when inferring shape distributions from sparse photometry.

*Unified Astronomy Thesaurus concepts:* Asteroids (72); Surveys (1671); Asteroid rotation (2211)

*Supporting material:* machine-readable table

## 1. Introduction

Approximately 95% of minor planets are found in the main asteroid belt between Mars and Jupiter. Minor planets can be considered to be remnant material dating back to the initial formation of the solar system; hence, the study of their rotational evolution can give important insight into the early beginnings of the solar system. The majority of known asteroid rotation periods are determined through ground-based observing; hence, deriving very long rotation periods is a nontrivial task. A more complete and less biased sample of long rotation periods will be highly beneficial for understanding the mechanisms driving rotational evolution within our solar system. The primary mechanisms affecting the rotation of main-belt asteroids are collisions and the Yarkovsky–O’Keefe–Radzievskii–Paddack (YORP) effect.

Collisions between asteroids can affect their orbital and spin properties. Major collisions may result in the catastrophic disruption of one or both of the objects (Nesvorný et al. 2002). Subcatastrophic collisions in aggregate may also cause changes in rotation period or, in some cases, induce nonprincipal axis rotation, causing objects to tumble. For small objects, these collisions may happen with greater frequency than the timescale required to damp this motion back to principal axis rotation. Subcatastrophic collisions could therefore be a driving mechanism producing small tumblers (Paolicchi et al. 2002).

The YORP effect can increase or decrease the spin rate of asteroids and meteoroids due to the action of thermal torques.

The anisotropic radiation emitted from an asymmetric object gives a net torque acting to cause an increase or decrease in the spin rate of the object dependent on the shape of the object, hereafter referred to as YORP spin-up/spin-down (Bottke et al. 2006). The change in spin states due to YORP is the accepted explanation for the difference in spin distributions between large and small asteroids. For large asteroids, the distribution of their rotation rates approximates a Maxwellian distribution, while in the small-body population with diameter  $D < 200$  m, the distribution is non-Maxwellian, and there has been shown to be an abundance of fast and slow rotators (Pravec & Harris 2000; Pravec et al. 2002). YORP spin-up is considered to be a mechanism behind the rotational fission of small asteroids, so similarly, we may consider YORP spin-down to be a potential mechanism behind slow rotators. Ascertaining the true difference between the abundances of slow rotators in these populations will be a key puzzle piece when understanding the rotational evolution of the solar system.

At the time of writing, there were 619,150 numbered minor planets, according to the Minor Planet Center, with over a million total known minor planets. Only a small fraction of these objects have known rotational properties, with 29,183 objects having reported rotation periods according to the Light Curve Database (LCDB; Warner et al. 2009). Note that this total includes periods derived from sparse sky surveys, including previous work on Transiting Exoplanet Survey Satellite (TESS) data by Pál et al. (2020). Figure 1 shows the rotation periods of all main-belt asteroids plotted against diameter as recorded in the LCDB, last updated in 2019 September (an update before TESS data from Pál et al. 2020 was added). This plot has been constrained to objects that have been assigned a quality code  $U \geq 2$ . The quality code is assigned according to the reliability of the period result

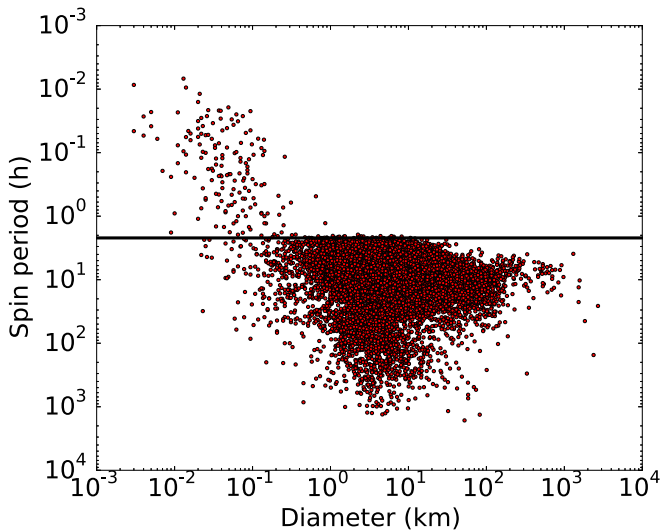


**Figure 1.** Plot of rotation period against diameter for all objects in the LCDB with quality code  $\geq 2$ -. The data are from Warner et al. (2009). Note that the data here are from 2020, before the addition of any other periodicities from TESS.

obtained. A value of  $U = 1$  is assigned for a period determined from a light-curve fragment that cannot be considered reliable,  $U = 2$  corresponds to a result from partial light curves with a period value known within an uncertainty of 30%, and  $U = 3$  is assigned to accurate results from full light-curve coverage (Warner et al. 2009).

Observing individual asteroids when determining rotation periods requires a time investment proportional to the rotation period of the object. For objects with long periods ( $P > 100$  hr), this time investment is likely to be prohibitive when telescope time is allocated. For these objects, we instead must look to sky surveys and archival data. For this reason, we also expect that the sample of known slow rotators is an underrepresentation of the true proportion of objects with these rotational properties. To that point, the longest known rotation period for a minor planet in the LCDB at the time of writing was  $P = 1880 \pm 595$  hr. Erasmus et al. (2021) showed rotation periods as long as  $P > 4000$  hr derived using archival data from the Asteroid Terrestrial Last-impact Alert System. A more complete understanding of these objects will yield great insight into the rotational and dynamical evolution of these objects. Although the primary mission of TESS is the study of exoplanets, over the course of the mission lifetime, tens of thousands of main-belt asteroids will enter the field of view, primarily in the camera pointing closest to the ecliptic. This provides an opportunity for an untargeted survey of main-belt asteroids, whose sky motions and magnitudes are well suited to TESS observations. In Section 2, we describe TESS, and in Section 3, we detail our photometric extraction. Our period determination method, overview of results, and period validation are described in Sections 4–6, with our main results presented in Section 7.

## 2. TESS

The primary science goal of TESS is the search for exoplanets transiting bright and nearby stars (Ricker et al. 2016). The satellite is situated in a highly elliptical 13.7 day orbit around the Earth. TESS observes with four wide-field optical cameras (each consisting of four  $2k \times 2k$  CCDs) with a

total field of view for each sector of  $24^\circ \times 90^\circ$ , with 13 sectors (pointings) in the southern ecliptic hemisphere scheduled for year 1 and a further 13 in the northern hemisphere in year 2. Each pointing will be observed for an interval ranging from 1 month to 1 yr, with the longest observing epochs near the ecliptic poles, which are continuously observed through the different pointings. Individual frames are taken every 2 minutes and stacked into full-frame images (FFIs) covering 30 minutes. The point-source magnitude range of the FFIs approximately corresponds to  $8 < V < 17$ , with  $21''$  pixels.

These data are particularly valuable in determining rotation periods and lower-limit elongations for a large population of asteroids. The study of sparse photometry for an untargeted survey has been carried out in the past using ground-based telescopes (McNeill et al. 2016; Cibulková et al. 2018). The key difference between these past studies and data from TESS is the space-based nature of the satellite, allowing for much longer baseline observations of asteroids without interruption by daylight. This, along with the long intervals during which the survey points at a given sector, has made this a unique opportunity to obtain observations of slow-rotating asteroids—bodies with periods longer than 100 hr that cannot be easily observed with classical observing and ground-based telescopes. The upper limit on derivable rotation periods is determined by the temporal extent of the observations for a given object, i.e., the total span of the TESS observations for an object. TESS is currently operating an extended mission, having completed Cycle 3 and carrying out Cycle 4 observations.

## 3. Extracting Photometry from TESS

The FFIs of TESS Cycle 1 were obtained using the bulk download services provided at the Barbara A. Mikulski Archive for Space Telescopes. The FFIs are identified by the sector and camera of the image; each downloaded FITS data cube is split into four separate flat FITS files according to their CCD identifiers. The background has been subtracted from each frame. The background has been measured as the median derived in a  $100 \times 100$  pixel cell and its eight neighboring cells utilizing a  $3\sigma$  sigma-clipping rejection using `astropy.photutils`.

From preprocessed frames within a sector–camera–CCD combination, 50 evenly temporally distributed frames are selected to generate a median background template for this sector–camera–CCD combination. The even spacing across time is necessary to capture systematic changes in the telescope pointing or artifacts changing with time due to nearby bright sources. The template image is subtracted from each frame in the corresponding sector–camera–CCD combination to remove static sources from the images. Due to the aforementioned systematics, image artifacting is introduced, primarily in close proximity to bright sources. In order to best minimize the effect of this on the output photometry, we create an image mask that covers these artifacts in each frame. The image mask is produced by convolving a  $5 \times 5$  pixel mask with those points that have pixel values less than the local median background minus three times the local background rms around the pixel location. The size of the pixel mask is chosen to conservatively mask the remaining flux from insufficiently subtracted background sources.

### 3.1. Target Identification

We first identify candidate asteroids that could be present in any CCD of the sector–camera combination by cross-referencing their positions with the coordinates of the telescope’s pointing. For this purpose, ephemerides of all known asteroids are calculated for the median epoch of all available observations for the given sector. Any asteroid within a  $25^\circ$  radius of the sector–camera center position and with a visual magnitude brighter than 20 is considered a candidate. Orbit calculations are performed using OpenOrb (Granvik et al. 2009) via the Python extension pyoorb and sbpy.data.Orbit (Mommert et al. 2019). Orbital elements used in this calculation are obtained from the Minor Planet Center orbit file MPCORB.DAT. Ephemerides are calculated relative to the geocentric location; this may introduce uncertainties in the position of near-Earth asteroids but does not significantly affect main-belt asteroids, which make up the vast majority of our targets. Additional uncertainty is introduced by the offset of the orbital element epoch from the actual epoch of the observations. In order to compensate for these uncertainties, a search cone (radius of  $25^\circ$ ) much larger than the actual field of view (radius of  $\sqrt{2} \cdot 12^\circ$ ) has been chosen. This approach was chosen over a more accurate ephemeris calculation in order to improve the computational performance of this search.

The second step obtains highly accurate ephemerides for each of the candidate asteroids. Ephemerides for each candidate were obtained using astroquery.jplhorizons (Ginsburg et al. 2019) from the JPL Horizons service accounting for the actual position of TESS and the time of the observations. Rejecting asteroids with positions outside the field of view of the CCD, visual magnitudes less than 20, and positional uncertainties greater than  $1''$ , this method builds a catalog of asteroids that are most likely to be found in the corresponding CCD. Finally, forced aperture photometry is performed on the accurate positions of asteroids identified through this method.

### 3.2. Aperture Photometry

Photometry is carried out for moving objects using forced aperture photometry using astropy.photutils. The target flux is measured in a circular aperture with a radius of 2 pixels. This size has been chosen to include a significant fraction of the target flux (a  $2 \times 2$  pixel aperture centered on a point source includes 90% of the total target flux<sup>6</sup>). The background is measured as the median pixel value within an annulus with an inner radius of 4 pixels and an outer radius of 8 pixels. Masked pixels are ignored in the photometric measurement. Uncertainties are estimated as the rms of the target’s Poisson noise in units of photons, the background noise across the target aperture, and the annulus that was used to estimate the sky background. The resulting photometry is written to a file on a per-object basis. In addition to positions and photometric properties, a flag indicates whether the aperture is affected by a pixel mask, enabling the quick identification of unreliable photometric measurements.

### 4. Period Determination

To derive the rotation period for each asteroid, we use the generalized Lomb–Scargle periodogram (Zechmeister & Kürster 2009), which accounts for photometric uncertainties in the

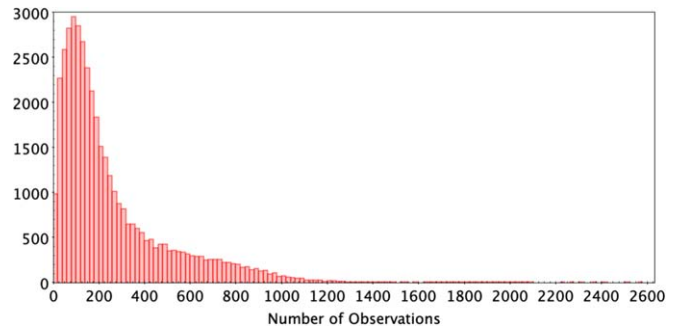


**Figure 2.** Histogram showing the number of observations per object across TESS Cycle 1. The y-axis in this figure shows the raw number of objects in each bin.

measured magnitudes. This method also fits for the mean of the distance and phase-corrected data rather than simply assuming that it is identical to that of the fitted sine curve as in the standard Lomb–Scargle algorithm. Note that we assume a standard value for the slope parameter,  $G$ , of 0.15 when correcting for the phase angle for all objects due to limited phase-angle coverage from TESS data alone. For each object, we probe a range of rotational frequencies,  $X < \omega < Y$ , and obtain the best fit to the observed data through  $\chi^2$  minimization. We assume that the variation in brightness in these light curves is due to geometric and shape effects rather than surface features and therefore assume the most likely period to be twice the best-fit period from our Lomb–Scargle periodogram. To derive the periods, we used the generalized Lomb–Scargle implementation outlined in Gowanlock et al. (2021). For each object, we searched light-curve periods in the range of 0.0416–17 days, corresponding to asteroid rotational periods of 2–816 hr. The search was carried out over a uniform frequency grid having  $N_f = 7 \times 10^5$  frequencies. From synthetic testing, we found that the cadence of the TESS observations is not sensitive to shorter periods; hence, we consider valid solutions only where the derived period is  $3 < P < 0.9(t_{\text{window}})$  hr, where  $t_{\text{window}}$  is defined as the temporal extent of the observations of a given object. In cases where no strong signal emerged, there is a systematic signal corresponding to the full observing window. We filter these values out along with anything within 10% of the observing window in order to remove this effect.

### 5. Results

Across Cycle 1 of TESS, we extracted photometry for 37,965 known minor planets, with 28,878 meeting our criteria of a minimum of 50 observations after sigma-clipping the data to remove outliers; in this process, data points farther than  $3\sigma$  from the mean value are removed from consideration. Figure 2 shows a histogram of the number of observations per object across Cycle 1. We derive the best-fit rotation period for each object, and we present our methodology for assessing the likelihood of each solution being correct. Considering only objects with 200 or more detections and a derived rotation period within our defined boundary of  $3 < P < 0.9(t_{\text{window}})$  hr, we have 10,470 objects; this is the sample used to display distributions later in the paper. A more complete examination of this confidence testing is found in Section 6. Figure 3 is a typical example of a TESS light curve where we consider the rotation period, in this case,  $P = 4.989$  hr, to be reliable. The Lomb–Scargle periodogram for this object is given in Figure 4.

<sup>6</sup> <https://heasarc.gsfc.nasa.gov/docs/tess/the-tess-space-telescope.html>

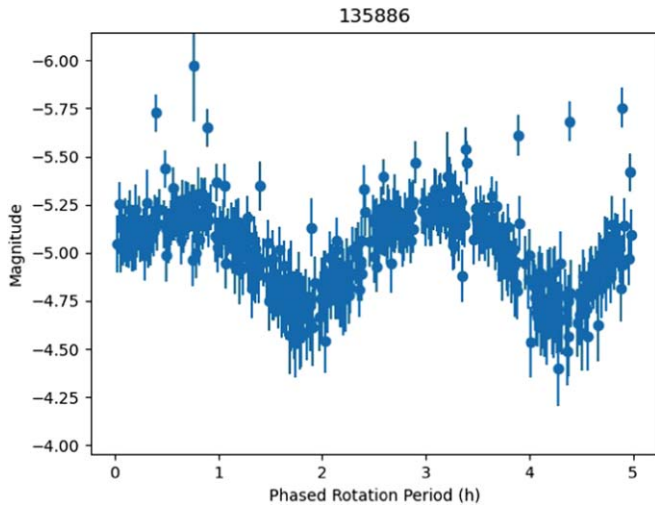


**Figure 3.** TESS light curve for asteroid 135886 in instrumental magnitudes corrected for distance and phase angle (i.e., “absolute” instrumental magnitudes). The rotational phase of the object is scaled from zero to  $P$ , where  $P$  is the derived rotation period of the object.

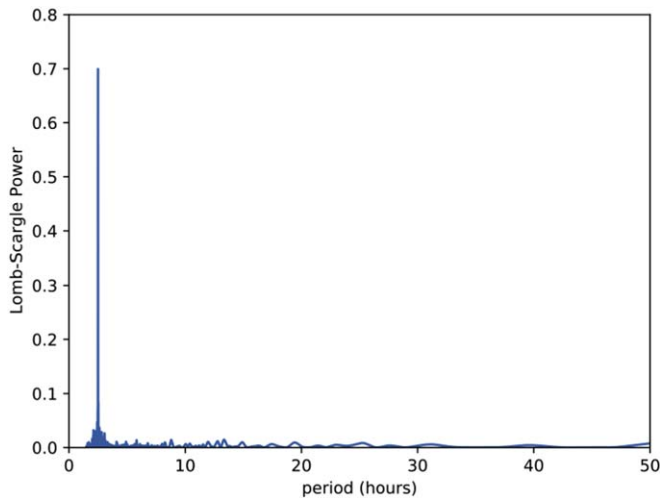


**Figure 4.** Generalized Lomb–Scargle periodogram obtained from period analysis for 135886.

Table 1 contains all objects for which there were  $>200$  detections. Full tables are available on the Advanced Research Computing Data Portal<sup>7</sup> and at CDS via anonymous ftp to cdsarc.u-strasbg.fr (130.79.128.5) or via the VizieR archive server.<sup>8</sup>

## 6. Period Validation

### 6.1. Synthetic Data Testing

In order to test the fidelity of our approach and solutions, we created a population of synthetic asteroids with known properties against which both our derived properties and algorithmic success can be compared. The creation of this synthetic asteroid population is described in detail in the Appendix of Trilling et al. (2023); we summarize the key elements here.

For this project, our synthetic asteroid catalog consisted of 10,000 objects. Each object is assigned a light curve. Each object’s light-curve period is drawn randomly from a lognormal distribution whose peak is near 6 hr, similar to the distribution found in the LCDB. Similarly, each object’s light-curve amplitude is drawn randomly from a lognormal distribution whose peak is near 0.4 mag, again similar to the distribution found in the LCDB. Each object is assigned an observing window length in the range of 0–27 days from a reversed lognormal distribution (peak at greater values, long tail to smaller values) that is similar to the distribution of observing window lengths for real asteroids observed by TESS.

The observational record for each object is then created. The initial light-curve phase is chosen randomly. The object is “observed” every 30 minutes—the TESS observational cadence—using the assigned light-curve period and amplitude. We then assign errors to this “measurement.” We randomly draw two values from a Gaussian distribution with a width of 0.1 mag, similar to the distribution of errors for real asteroids in the TESS data set. Each measurement is offset from its nominal value by the first of these errors and then assigned an error bar of the second of these values, in order to capture the true scatter of measurements in the TESS data records.

Each object is then randomly assigned a number of (synthetic) observations in the range of 0–1000 from a lognormal distribution whose peak is near 100 observations and that is similar to the distribution of the number of observations of real asteroids made by TESS. Finally, we randomly remove data points from each asteroid’s observational history to reach this target number of observations in order to simulate individual TESS measurements being corrupted due to close passage to a background source, cosmic-ray contamination, etc. The result is a distribution of window lengths and number of observations that is very similar to that of real asteroids observed by TESS.

For each object, we use the machinery described above to derive the light-curve period and amplitude, and we compare our derived results to the (known) input values. Overall, the match rate is very high, and we obtain a correct rotation period in 99% of cases where more than 200 (synthetic) detections were made.

A similar process was carried out focusing on objects with fast rotators to assess the viability of deriving relatively short rotation periods from TESS data. We find that for objects with rotation periods of less than 3 hr, the proportion of correct periods derived from synthetic data was only 35%. We therefore urge caution when relying on any rotation periods derived from TESS within this range.

### 6.2. Comparison with LCDB

We do not consider the derived periods from TESS to be uniformly reliable. Instead, we expect that the confidence in the derived period should increase with the total number of observations and in the normalized Lomb–Scargle power of the periodogram fit. Figure 5 shows a heat map of the proportional matches between the TESS data and the LCDB where entries have a quality code  $U=3$ , implying only unambiguous solutions. We present the cumulative form of the derived heat maps throughout this work. If a differential form is used, many of the cells are sparse, and the overall clarity of the figure is lessened. The two axes here are the normalized power of the Lomb–Scargle signal for the best fit in the periodogram and the

<sup>7</sup> [https://rcdata.nau.edu/snaps/published\\_datasets/TESSC1/](https://rcdata.nau.edu/snaps/published_datasets/TESSC1/)

<sup>8</sup> <http://cdsarc.unistra.fr/viz-bin/cat/J/AJ>

**Table 1**  
TESS Rotation Periods (Abbreviated for Draft Paper)

MPC Desig.	Derived Period (hr)	Period $\sigma$	Amp (mag)	Confidence (Exact)	Confidence (Incl. Alias)	Matches Pál et al. (2020)
1000	9.476	0.001	0.251	0.940	0.987	...
100003	18.707	0.014	0.817	0.848	0.908	N
100012	14.324	0.002	0.076	0.836	0.925	...
100118	25.736	0.011	0.192	0.790	0.882	...
100134	139.462	0.392	0.296	0.825	0.911	N
100169	12.897	0.004	0.166	0.743	0.815	...
100179	69.923	0.155	0.189	0.743	0.815	N
100199	120.778	0.217	0.257	0.873	0.963	N
100293	676.645	12.566	0.146	0.774	0.855	...
100327	7.571	0.001	0.227	0.869	0.965	...
10035	16.748	0.010	0.077	0.743	0.815	...
100359	31.424	0.015	0.133	0.790	0.882	N
100430	8.850	0.003	0.123	0.783	0.849	...
100436	34.273	0.040	0.602	0.814	0.880	...
100438	19.144	0.011	0.793	0.848	0.908	...
100461	54.797	0.037	0.219	0.790	0.882	N
100464	23.317	0.021	0.958	0.814	0.880	...
100491	14.533	0.004	0.332	0.790	0.882	N
100495	513.814	5.534	0.218	0.789	0.860	N
100585	26.565	0.004	0.508	0.907	0.980	Y
10061	10.132	0.002	0.532	0.874	0.959	N
100643	2.822	0.001	0.212	0.779	0.866	...
100656	12.041	0.001	0.486	0.937	0.984	Y
100661	470.083	6.557	0.217	0.735	0.802	...
100664	16.268	0.007	0.129	0.783	0.874	...
100714	27.491	0.018	0.248	0.820	0.900	...
100753	4.731	0.001	0.282	0.851	0.929	Y
100758	15.671	0.017	0.362	0.841	0.913	...
100766	25.348	0.022	0.546	0.864	0.928	...
10080	7.052	0.001	0.188	0.937	0.984	...
100812	15.151	0.008	0.359	0.783	0.849	...
100850	5.464	0.001	0.448	0.894	0.949	Y
10086	595.987	3.917	0.153	0.790	0.882	...
10087	8.580	0.001	0.248	0.880	0.967	...
100877	422.887	4.157	0.227	0.820	0.900	N
100980	39.856	0.048	0.563	0.874	0.959	...
10101	6.850	0.001	0.456	0.940	0.987	Y
10103	330.243	2.961	0.369	0.873	0.963	N
101144	26.257	0.042	0.538	0.841	0.913	...
101168	80.001	0.183	0.268	0.735	0.802	N
101169	78.661	0.251	0.931	0.921	0.966	N
10117	6.881	0.001	0.482	0.930	0.985	Y
10118	156.401	0.272	0.195	0.790	0.882	N
10128	9.571	0.001	0.153	0.929	0.982	Y
101286	33.025	0.020	0.138	0.790	0.882	N
10134	5.534	0.001	0.211	0.929	0.982	Y

(This table is available in its entirety in machine-readable form.)

total number of observations for the object. We assign a confidence to the best-fit rotation period according to its position in this heat map, as seen in Table 1. Aliased solutions are defined as those where the TESS and LCDB periods differ by a factor of  $0.5\% \pm 3\%$  or  $2\% \pm 3\%$ .

From the extracted TESS objects, we select those that have been reported in the LCDB with a quality score of  $U \geq 2$ . We find that 10,039 of the TESS objects have been reported. Restricting this to objects with more than 200 photometric measurements and a normalized Lomb–Scargle power greater than 0.2, we compare our derived periods to the 1219 overlapping periods reported in the LCDB and present Figure 6, showing the derived TESS period plotted against the literature LCDB period for the relevant objects. From this

sample, we also removed all objects where the period solution was within 10% of the observing window for that object. The period solutions in this period space are not reliable and are driven by the length of the overall observing window. We define an exact rotation period match when our derived TESS period and the LCDB period of a given object are within 3% of one other. Aliased matches also include values where the derived TESS and LCDB periods are different by a factor of 2. We find that 85% of our overlapping rotation periods are exact matches to the LCDB, with that proportion rising to 91% when aliased matches are also considered. These cells are indicated with a black outline in Figure 5.

The resulting heat map constructed here matches our expectations from the synthetic data. We find that the match

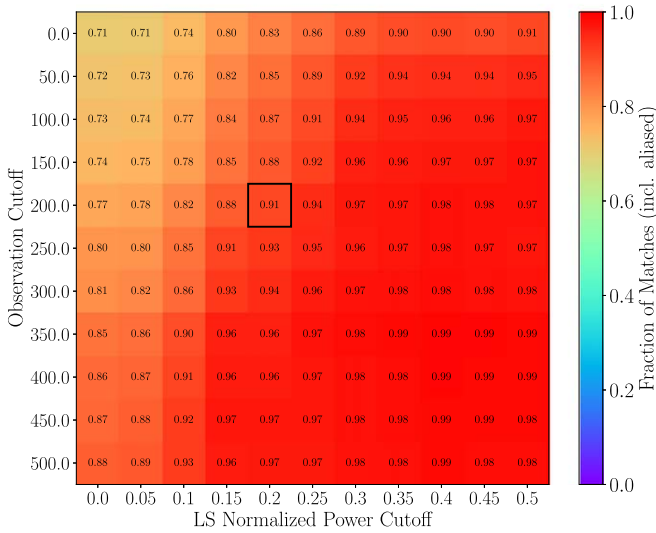
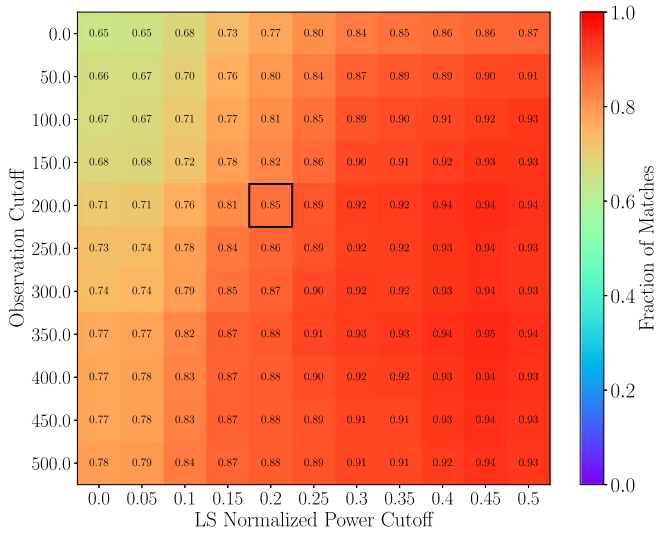


**Figure 5.** Fraction of asteroid rotation period matches between TESS and LCDB ( $U = 3$ ) as a function of the observation and Lomb–Scargle normalized power cutoff. An object falls within a bin if it has at least the number of observations and Lomb–Scargle power as shown on the vertical and horizontal axes, respectively. (Top) Exact matches. (Bottom) Exact and aliased matches. The black outlined cells show the cases where there are more than 200 data points and the normalized Lomb–Scargle power is greater than 0.2, as discussed in the text.

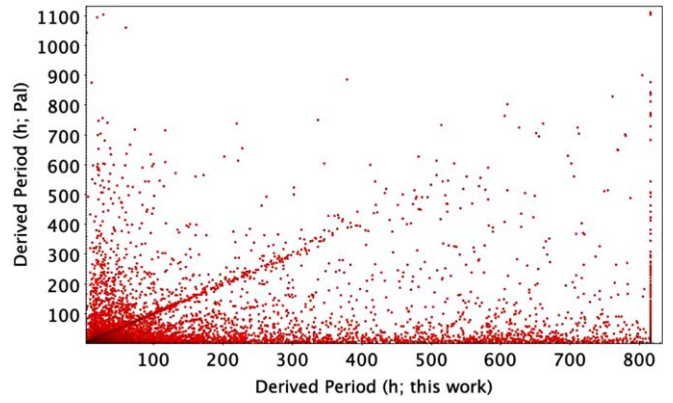


**Figure 7.** Comparison of the best-fit rotation periods reported by Pál et al. (2020) with the best-fit periods obtained in this work for the same objects. Note that no quality cutoff or consideration is made at this stage.

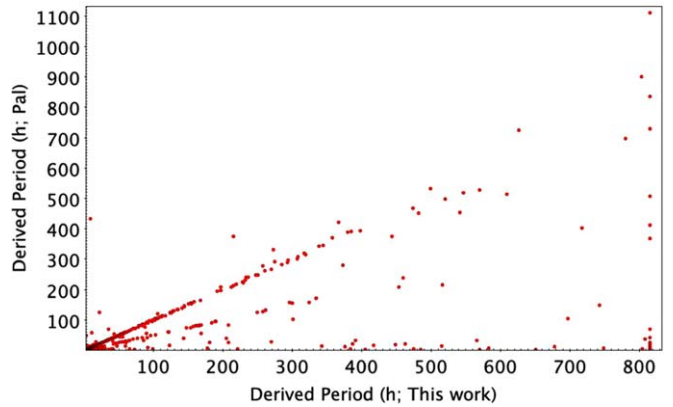


**Figure 8.** Same as Figure 7 except only for objects with more than 200 photometric detections after quality control.

rate for correct periods is between 71% and 94% for objects with more than 200 observations, depending on the Lomb–Scargle periodogram signal strength. This is a lower match rate than found from our synthetic testing, which is not surprising given the additional factors present in the real TESS data that were not present in the synthetic testing, e.g., stray-light scatter under the Sun shield of the satellite. Additionally, systematic errors due to the TESS facility are not accounted for in the synthetic data testing.

### 6.3. Comparison to Pál et al. (2020)

Pál et al. (2020) carried out an earlier study of moving objects within TESS Cycle 1 and reported 9912 asteroid light curves. Figure 7 shows a direct comparison between the best-fit rotation periods from this work and the values from Pál et al. (2020). No quality or confidence cutoffs were made prior to the generation of this plot.

As can be clearly seen, there is a significant discrepancy between the two sets of values. In order to assess this in line with our own quality expectations, we will now only look specifically at objects with more than 200 individual photometric measurements and a normalized Lomb–Scargle power greater than 0.2. We find 1119 objects meeting these criteria with rotation periods derived in both studies.

Figure 8 shows a comparison between the derived periods in this work and in Pál et al. (2020) for these 1119 objects. We specifically examine the 619 objects that have their LCDB

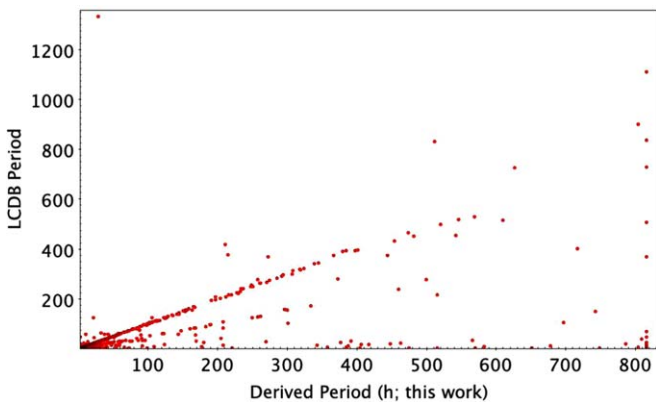


**Figure 6.** Comparison of the derived periods from this work with the literature periods stored in the LCDB for those objects with greater than 200 detections within TESS.

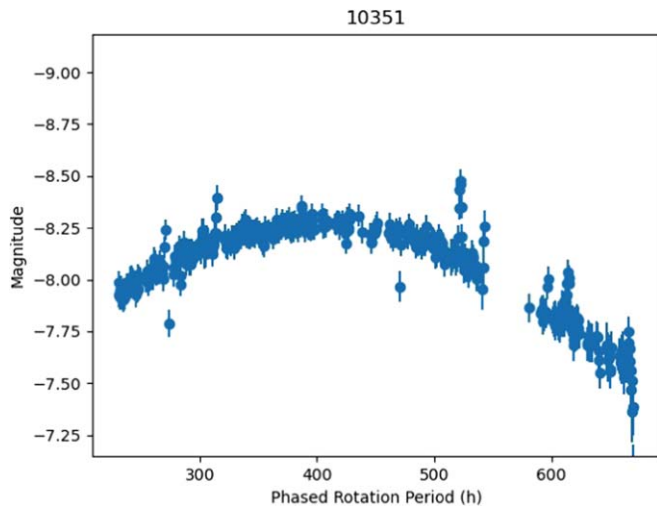


**Figure 9.** Light curve from this study for asteroid 10351. As no period solution was derived, the  $x$ -axis here shows the temporal extent of the observations with no folding.

entries based on the derived period by Pál et al. (2020). Of these, our solutions agree with Pál et al. (2020) in 80% of cases. Of the remainder, we first look at those objects where periods were derived from incomplete light curves. Pál et al. (2020) found that asteroid 10351 has a rotation period  $P = 367.413$  hr (this has subsequently been given a listing in the LCDB with quality code  $U = 2$ ). From our own study, this object was marked as having only a partial light curve, as no clear evidence of a full rotation was seen in the light curve. Figure 9 shows the light curve produced for this object in this work.

Figure 10 shows the same data folded to  $P = 367.413$  hr. This clearly does not meet the specified criteria for a quality code of 2, i.e., that the period is likely to be correct within 30%. As this putative light curve is discontinuous, this folding period of  $P = 367.413$  hr clearly cannot be correct. We consider objects for which both Pál et al. (2020) and this work find period solutions in independent agreement to be reliable and these objects, as well as having their assigned confidence values from this work, are flagged accordingly in Table 1.

Where our period and Pál et al. (2020) are in agreement, we believe that these solutions should be considered to be reliable within the confidence limit that we have set. As stated in Section 6.1, we find that periods shorter than 3 hr derived from TESS should be considered unreliable; we have excluded such periods from our results.

#### 6.4. Conclusions of Period Validation

To summarize, we have tested our period-finding methodology using synthetic TESS data before conducting an analysis of the Cycle 1 data for comparison with both literature values and Pál et al. (2020).

1. From synthetic data, we find that we would expect to obtain the correct period in 99% of cases where more than 100 individual measurements were made.
2. We find that our derived periods match literature values in 85% of cases where there are 200 photometric observations from TESS, assuming a cutoff in the generalized Lomb–Scargle periodogram power of 0.2.

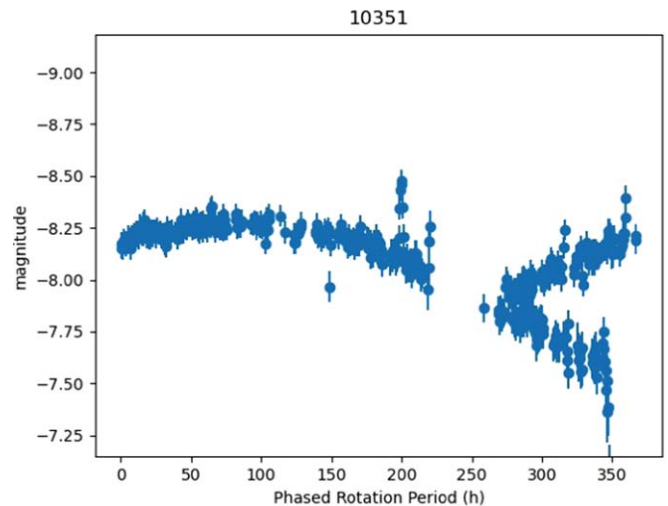


**Figure 10.** Light curve from this study for asteroid 10351 folded to the period solution of Pál et al. (2020).

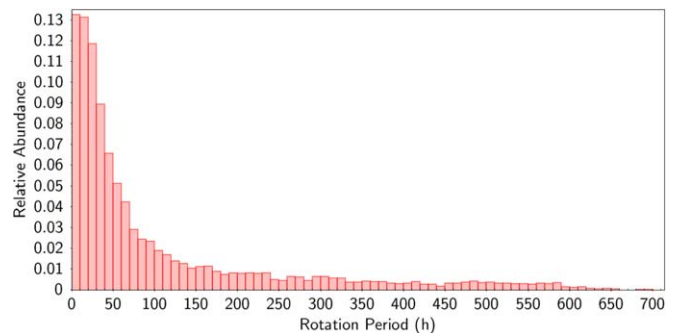


**Figure 11.** Linear histogram showing the derived rotation periods for 10,470 asteroids with more than 200 detections and periods within our acceptable boundaries across TESS Cycle 1.

3. We find that our derived periods match those derived independently by Pál et al. (2020) in 80% of cases where the objects appear in both works; there are, however, numerous cases of significant disagreement.

## 7. Science Results

### 7.1. Rotation Period Distribution

A goal of this project was to derive a more complete picture of the proportion of slow rotators among main-belt asteroids. The observing strategy of TESS allows for sensitivity to derived periods between 3 hr and an upper limit governed by the time span over which the object was observed (see Figure 6). This allows for the proportion of slow rotators with rotation periods of order hundreds of hours to be determined. This will be highly informative for statistical determinations of the shape distribution for asteroids, as objects with very slow rotation periods are likely underrepresented in these models due to the observational biases against them in real data. Linear and log histograms of the derived period distribution are given in Figures 11 and 12; note that the same data are shown in each, with the difference being the linearity of the  $x$ -axis. As we are unaffected by aliases introduced by diurnal, ground-based observing, these results can be used to clearly see that the proportion of objects with periods equal to integer multiples of 12 hr is just as expected from a smooth distribution.

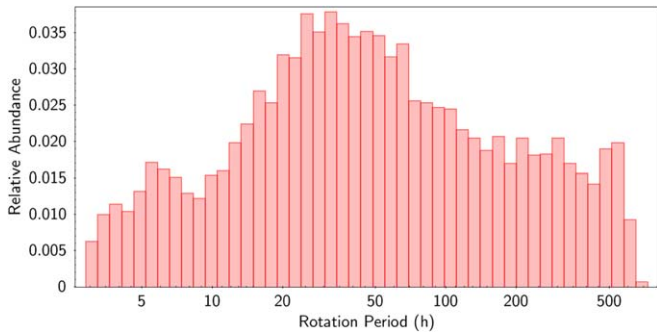


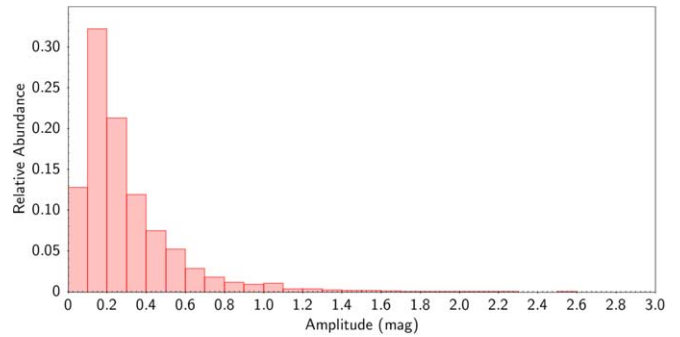
**Figure 12.** Log histogram showing the derived rotation periods for asteroids across TESS Cycle 1.

### 7.2. Light-curve Amplitudes and Shape Implications

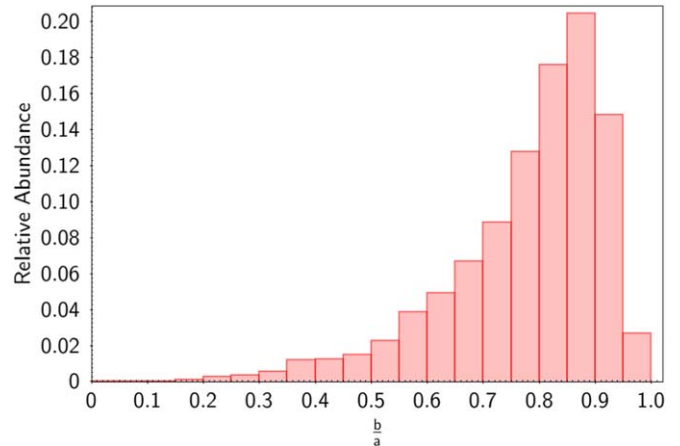
Light-curve amplitude can be considered a simple first-order analog for the elongation of an object, assuming that all light-curve variation comes from the varying projected area of the object about its rotation. To determine the estimated amplitude for asteroids found in TESS, we fit a simple sine curve to the data based upon the derived rotation period. Alternative methods would include taking a running mean of the light curve or fitting a more complex Fourier transform to the data; however, we consider the former too primitive, and the latter offered no clear increase in fidelity while reducing the overall total of amplitude solutions. By necessity, the method used required a reliable period solution in order to determine the amplitude.

Figure 13 shows the distribution of derived light-curve amplitudes from our targets in Cycle 1. Two objects with extreme amplitudes were discarded from this sample after spot-checking, as the extreme amplitudes in these cases were due to data contamination. Both light curves showed extreme increases in magnitude that were later shown to be due to a source in the original image being poorly masked. Taking only objects for which more than 200 detections were made and the Lomb–Scargle solution yielded a power greater than 0.2, we find that 5% of the objects have amplitudes greater than 1.0 mag. In previous statistical work in McNeill et al. (2016), we estimated that this proportion should be closer to 0.2%; as the TESS processing has largely been automated, we recommend this lower value be used as an estimate for this value among main-belt objects. This is much higher than our previous result, and because of possible contamination, this TESS result may be an overestimate, with the true result lying somewhere between these limits. It is the recommendation of the authors that data users always independently spot-check high-amplitude values for this reason.

Figure 14 shows the implied axis ratio of the objects assuming no required correction for the phase-angle amplitude (PAA) effect. This effect inflates the apparent amplitude of a light curve with increasing phase angle (Zappala et al. 1990). Note that the dearth of spherical objects is due to the bias that we require a reliable period fit to determine amplitude and that this is difficult for objects with light-curve amplitudes comparable to the typical TESS photometric uncertainty of around 0.05–0.1 mag. Assuming a fixed spin pole latitude of  $50^\circ$ , we find that our mean axis ratio here is in agreement with the values obtained by McNeill et al. (2016),  $b/a = 0.85 \pm 0.13$ , who similarly determined shape distributions for kilometer-sized main-belt asteroids without accounting for



**Figure 13.** Histogram of the derived amplitudes from Cycle 1 of TESS for 10,470 objects. The amplitudes presented here are uncorrected for the PAA effect.



**Figure 14.** Histogram of the apparent  $b/a$  axis ratios for asteroids as suggested by their light-curve amplitudes. The relative lack of spherical objects represented in this plot is due to biases discussed in the text. We find that 5% of the objects have high-amplitude light curves corresponding to  $b/a$  mean axis ratios of  $<0.4$ .

PAA effects. It will be important to properly account for the proportion of slow rotators in a given population in order to ensure that this result is reliable. Underestimating the proportion of slow rotators will likely lead to a bias toward more spherical shapes, as these may be mistaken for mostly flat light curves with shorter rotation periods.

Using the method of McNeill et al. (2016), we take a population and apply their shape distribution model assuming three cases: (i) no slow rotators, (ii) 10% slow rotators, and (iii) 50% slow rotators (an extreme case). We find that in the case of 10% unaccounted-for slow rotators, this produces an uncertainty in the average derived axis ratio of 0.02, well within the errors of such modeling. In the extreme case, we find that an uncertainty of as much as 0.1 can be produced. Although the extreme case is highly unlikely, this emphasizes the need to properly account for slow-rotating objects when doing such work with sparse photometry.

### 7.3. Potential Trends with Size and Heliocentric Distance

Using the derived periods and amplitudes for objects with more than 200 observations, we investigate any trends with shape or rotational properties in the data set with semimajor axis and absolute magnitude. For semimajor axis, we consider two subpopulations, the inner main belt ( $2 \text{ au} < a < 2.5 \text{ au}$ ) and the outer main belt ( $3 \text{ au} < a < 3.5 \text{ au}$ ). For absolute



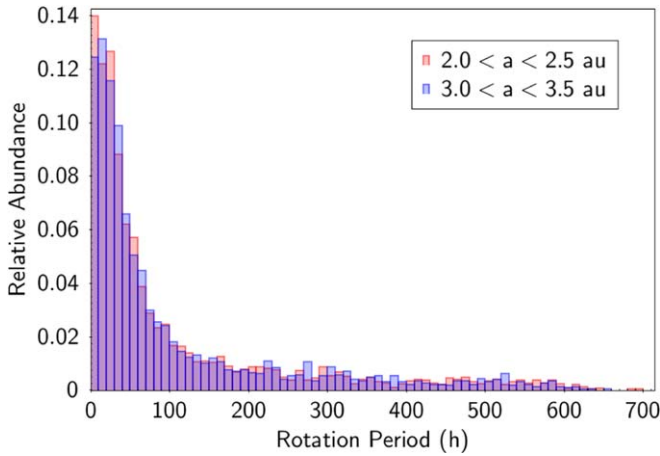


**Figure 15.** Histograms of the derived rotation periods for objects with more than 200 detections within Cycle 1. The red histogram describes the inner main belt at  $2 \text{ au} < a < 2.5 \text{ au}$ , and the blue histogram describes the outer main belt at  $3 \text{ au} < a < 3.5 \text{ au}$ .

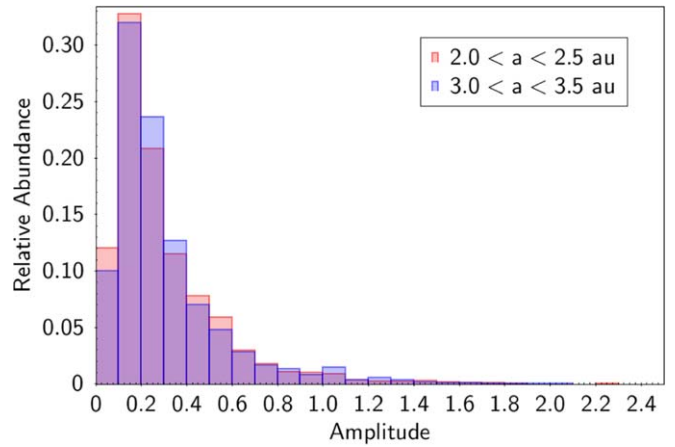


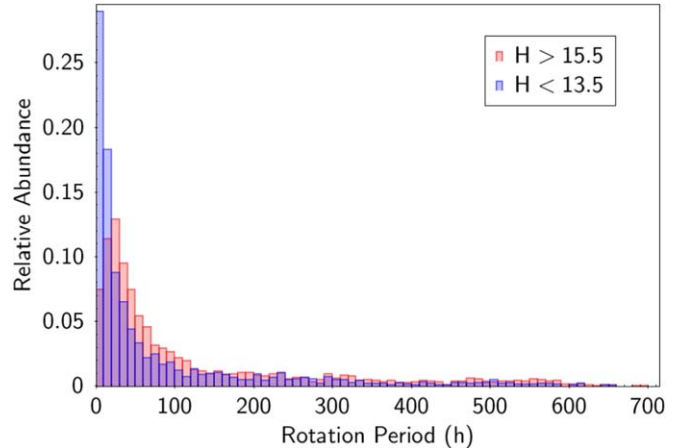
**Figure 16.** Histograms of the derived light-curve amplitudes for objects with more than 200 detections within Cycle 1. The red histogram describes the inner main belt at  $2 \text{ au} < a < 2.5 \text{ au}$ , and the blue histogram describes the outer main belt at  $3 \text{ au} < a < 3.5 \text{ au}$ .

magnitude, we split broadly into “large” objects with  $H < 13.5$  and “small” objects with  $H > 15.5$ .

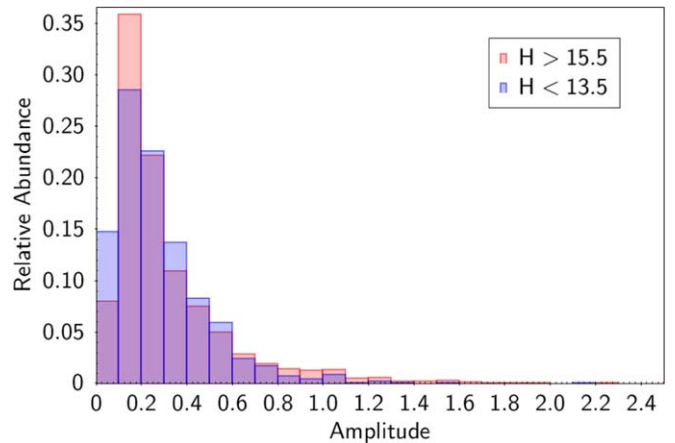
Looking first at semimajor axis, as shown in Figure 15, we find that there is no clear difference in the distribution of rotation periods between the inner and outer main belt. Carrying out the two-sample Kolmogorov–Smirnov (K-S) test on the two distributions produced a  $p$ -value of 0.62, suggesting that for this comparison, we cannot reject the null hypothesis that the two data sets are from a common distribution.

Figure 16 shows the distribution of derived light-curve amplitudes for the inner and outer main belt. A K-S test on these two distributions produced a  $p$ -value of 0.14, again suggesting that we cannot reject the null hypothesis in this case. Additionally, it is worth noting that observational biases will play a part in the amplitude distributions here; i.e., it will be easier to constrain low-amplitude solutions for objects that are closer than their counterparts in the outer main belt. This may suggest that debiased distributions may produce a higher  $p$ -value than the one obtained here, being more indicative of a common source distribution. For completeness, the K-S test was also carried out comparing each of these two ranges to the intermediate objects falling between our defined regions i.e.,  $2.5\text{--}3 \text{ au}$ . For both rotation period and amplitude, we find that, similar to the comparison of inner and outer main-belt objects, we cannot reject the null hypothesis in the comparisons of inner-to-intermediate or outer-to-intermediate.

Dividing the data by absolute magnitude,  $H$ , as a loose analog for size, we consider two subpopulations of the Cycle 1 data. We take objects with  $H < 13.5$  to be large objects ( $D \sim 7 \text{ km}$  assuming an albedo of 0.15) and those with  $H > 15.5$  to be small objects ( $D \sim 2 \text{ km}$  using the same assumed albedo). Figures 17 and 18 show the distributions of the derived rotation period and light-curve amplitude for these two subpopulations. We find the  $p$ -values from a K-S test for comparison between rotation period distributions and amplitude distributions to be  $0.02$  and  $2 \times 10^{-6}$ , suggesting that in each case, we can reject the null hypothesis that the distributions were drawn from a common source. For rotation period, we find that there is an abundance of shorter-period objects in the larger population compared to the smaller population and a slight abundance of slower rotators in the small population. To fully explore what the cause of this difference might be, it would be highly useful



**Figure 17.** Histograms of the derived rotation periods for objects with more than 200 detections within Cycle 1. The red histogram describes small objects with  $H > 15.5$ , and the blue histogram describes large objects with  $H < 13.5$ .



**Figure 18.** Histograms of the derived light-curve amplitudes for objects with more than 200 detections within Cycle 1. The red histogram describes small objects with  $H > 15.5$ , and the blue histogram describes large objects with  $H < 13.5$ .

to also have a complete sample of periods of  $<3$  hr within these size ranges, which this data set cannot reliably provide.

Trilling et al. (2023) derived rotation periods for objects observed by the Zwicky Transient Facility. From these data, an abundance of shorter rotation periods at larger sizes was observed, assuming the same definitions of “small” and “large” as this paper. This work also reported a comparative lack of sensitivity to short periods of  $P < 3$  hr preventing a complete sample of objects with these rotation rates.

Simplistically, it is possible that the relative abundance of faster rotators at large sizes may be caused by the YORP effect acting more efficiently on objects of smaller size and acting to increase/decrease their rotation periods. In such a case, it is possible that objects being “spun-up” could have their rotation period decrease below the sensitivity of our period determination from TESS. However, it is unclear how this mechanism would produce the distribution for smaller objects seen in Figure 17, where there is a clear decrease in abundance toward periods of less than 30 hr. The larger size range also represents a less collisionally evolved population, suggesting that some combination of collisional effects and YORP may explain this difference in rotational distribution.

For amplitude, we find that there are more low-amplitude (i.e., near-spherical) objects in the larger population; this is likely to be an observational bias, as low-amplitude solutions will be more easily constrained for brighter objects.

The K-S test was carried out comparing our defined large and small objects to the objects falling between these two ranges, i.e.,  $H = 13.5\text{--}15.5$ . For both rotation period and amplitude, we find that these comparisons produce incredibly small  $p$ -values of  $\ll 0.01$ , suggesting that we can also reject the null hypothesis, i.e., that both size ranges have the same period distribution, in these cases.

## 8. Conclusions

We have extracted photometric data for 37,965 minor planets observed by TESS during Cycle 1 operations. We have presented an examination of the reliability of the rotation period and light-curve amplitudes derived from each object based upon the number of detections and the normalized Lomb–Scargle power of our period fitting. This suggests that for those objects with 200 or more detections and a derived Lomb–Scargle power greater than 0.2, we have 85% confidence in that period. We have 3492 such highly reliable rotation periods. We compare and contrast our results with previous similar works and independently verify a series of periods first found by Pál et al. (2020); periods where both works are in agreement should be considered reliable. The period-finding capabilities of TESS and its relatively unaliased observing cadence represent an excellent diagnostic for verifying that periods obtained in ground-based observations are not, in truth, aliases. All of the photometry and results

catalogs are published online at the Advanced Research Computing Data Portal, [https://rcdata.nau.edu/snaps/published\\_datasets/TESSC1/](https://rcdata.nau.edu/snaps/published_datasets/TESSC1/), and CDS via anonymous ftp to cdsarc.u-strasbg.fr (130.79.128.5) or via the Vizier archive server, <http://cdsarc.unistra.fr/viz-bin/cat/J/AJ>.

## Acknowledgments


We thank the anonymous reviewer for the feedback that improved the overall quality of this manuscript. A.M. was supported by NASA Solar System Workings grant No. 80NSSC20K0864 and in part by the Arizona Board of Regents Regents Innovation Fund. M.G. was supported by the National Science Foundation under grant No. 2042155.

*Facility:* TESS

*Software:* astropy (Astropy Collaboration et al. 2013), SExtractor (Bertin & Arnouts 1996)

## ORCID iDs

Andrew McNeill  <https://orcid.org/0009-0005-9955-1500>

Michael Gowanlock  <https://orcid.org/0000-0002-0826-6204>

Michael Mommert  <https://orcid.org/0000-0002-8132-778X>

David E. Trilling  <https://orcid.org/0000-0003-4580-3790>

Joe Llama  <https://orcid.org/0000-0003-4450-0368>

## References

- Astropy Collaboration, Robitaille, T. P., Tollerud, E. J., et al. 2013, *A&A*, **558**, A33
- Bertin, E., & Arnouts, S. 1996, *A&AS*, **117**, 393
- Botke, W. F. J., Vokrouhlický, J., Rubincam, D. P., & Nesvorný, D. 2006, *AREPS*, **34**, 157
- Cibulková, H., Nortunen, H., Ďurech, J., et al. 2018, *A&A*, **611**, A86
- Erasmus, N., Kramer, D., McNeill, A., et al. 2021, *MNRAS*, **506**, 3872
- Ginsburg, A., Sipőcz, B. M., Brasseur, C. E., et al. 2019, *AJ*, **157**, 98
- Gowanlock, M., Kramer, D., Trilling, D. E., Butler, N. R., & Donnelly, B. 2021, *A&C*, **36**, 100472
- Granvik, M., Virtanen, J., Oszkiewicz, D., & Muinonen, K. 2009, *MAPS*, **44**, 1853
- McNeill, A., Fitzsimmons, A., Jedicke, R., et al. 2016, *MNRAS*, **459**, 2964
- Mommert, M., Kelley, M., de Val-Borro, M., et al. 2019, *JOSS*, **4**, 1426
- Nesvorný, D., Botke, W. F. J., Dones, L., & Levison, H. F. 2002, *Natur*, **417**, 720
- Pál, A., Szakáts, R., Kiss, C., et al. 2020, *ApJS*, **247**, 26
- Paolicchi, P., Burns, J. A., & Weidenschilling, S. J. 2002, Asteroids III (Tucson, AZ: Univ. Arizona Press), 517
- Pravec, P., & Harris, A. W. 2000, *Icar*, **148**, 12
- Pravec, P., Harris, A. W., & Michalowski, T. 2002, Asteroid Rotations (Tucson, AZ: Univ. Arizona Press), 113
- Ricker, G. R., Vanderspek, R., Winn, J., et al. 2016, *Proc. SPIE*, **9904**, 99042B
- Trilling, D. E., Gowanlock, M., Kramer, D., et al. 2023, *AJ*, **165**, 111
- Warner, B. D., Harris, A. W., & Pravec, P. 2009, *Icar*, **202**, 134
- Zappala, V., Cellino, A., Barucci, A. M., Fulchignoni, M., & Lupishko, D. F. 1990, *A&A*, **231**, 548
- Zechmeister, M., & Kürster, M. 2009, *A&A*, **496**, 577